LETTER

Structural basis of N^6–adenosine methylation by the METTL3–METTL14 complex

Xiang Wang[1]*, Jing Feng[1]*, Yuan Xue[1]*, Zeyuan Guan[1], Delin Zhang[1], Zhu Liu[2], Zhou Gong[3], Qiang Wang[1], Jinbo Huang[1], Chun Tang[2,3], Tingting Zou[1,4] & Ping Yin[1]

Chemical modifications of RNA have essential roles in a vast range of cellular processes[1–3]. N^6-methyladenosine (m6A) is an abundant internal modification in messenger RNA and long non-coding RNA that can be dynamically added and removed by RNA methyltransferases (MTases) and demethylases, respectively[2–5]. An MTase complex comprising methyltransferase-like 3 (METTL3) and methyltransferase-like 14 (METTL14) efficiently catalyses methyl group transfer[6,7]. In contrast to the well-studied DNA MTase[8], the exact roles of these two RNA MTases in the complex remain to be elucidated. Here we report the crystal structures of the METTL3–METTL14 heterodimer with MTase domains in the ligand-free, S-adenosyl methionine (AdoMet)-bound and S-adenosyl homocysteine (AdoHcy)-bound states, with resolutions of 1.9, 1.71 and 1.61 Å, respectively. Both METTL3 and METTL14 adopt a class I MTase fold and they interact with each other via an extensive hydrogen bonding network, generating a positively charged groove. Notably, AdoMet was observed in only the METTL3 pocket and not in METTL14. Combined with biochemical analysis, these results suggest that in the m6A MTase complex, METTL3 primarily functions as the catalytic core, while METTL14 serves as an RNA-binding platform, reminiscent of the target recognition domain of DNA N^6-adenine MTase[9,10]. This structural information provides an important framework for the functional investigation of m6A.

N^6-methyladenosine is a prevalent RNA modification in species including viruses, bacteria[11], yeasts[12], plants[13] and mammals[14,15]. It functions in multiple aspects of developmental regulation[16], the cell cycle[17], fate determination[18,19], and the heat shock stress response[20] by affecting aspects of RNA metabolism such as pre-mRNA processing[21], translation efficiency[22,23], transcript stability[24] and miRNA biogenesis[25]. Three distinct classes of protein factor are involved in the function of the m6A modification[3,5]: 'writers' (adenosine MTases)[6,7,16,26], 'erasers' (m6A-demethylating enzymes)[27,28] and 'readers' (m6A-binding proteins)[24,29]. The writers and erasers reversibly install and remove this modification, respectively, thereby generating a dynamic m6A landscape[5]. The readers, known as the YTH domain family[24,29], bind selectively to the m6A-containing sequence and contribute to the determination of RNA fate. Although the erasers and readers have been well characterized, the lack of structures of writers remains a major obstacle to the elucidation of the versatile functions of m6A.

In humans, two MTases, METTL3 (also known as MT-A70) and METTL14 participate in this modification as 'writers'[6,7]. Sequence analysis indicates that both proteins belong to the class I MTase family[30] (Extended Data Fig. 1) and they form a core catalytic complex that is regulated by an additional subunit, Wilms' tumour 1-associating protein (WTAP)[7,16,26]. Individually, METTL3 and METTL14 exhibit comparable weak MTase activity *in vitro*. However, the METTL3–METTL14 complex has much higher catalytic activity[6,7]. The mechanism by which the MTases functions synergistically awaits structural investigation.

To elucidate the mechanism of m6A methylation by the METTL3–METTL14 complex, we determined the crystal structure of the core METTL3–METTL14 complex comprising the MTase domain (METTL3, residues 369–570; METTL14, residues117–402) (Fig. 1a) in the space group $P4_12_12$, using bromide-based single-wavelength anomalous diffraction, at a refined resolution of 1.9 Å (Extended Data Table 1). Additionally, residues 200–204 in METTL14 could not be modelled. In the crystal, one METTL3 molecule and one METTL14 molecule form an antiparallel heterodimer in the asymmetric unit, resulting in an overall butterfly appearance with a width of approximately 40 Å and a length of approximately 70 Å (Fig. 1b).

We traced the METTL3 MTase domain and the METTL14 MTase domain, which is adjacent to the N-terminal α-helical motif (NHM) and to the C-terminal motif (CTM) with an phosphoserine at position 399 (Fig. 1b). The NHM extends across the MTase domain of METTL14 and to the MTase domain of METTL3. The MTase domain of METTL3 adopts a classic α–β–α sandwich fold comprising a mixed eight-stranded β-sheet with a strand order of β1↑, β8↑, β7↑, β2↑, β3↑, β5↓, β4↑ and β6↑ flanked by four α-helices (α1, α2 and α4 on one side, and α3 on the other side) and three 3_{10} helices (Fig. 1c). The overall structure of the METTL3 MTase domain primarily resembles that of the class I DNA N^6-adenine MTase[8,10,30] (Fig. 1c and Extended Data Fig. 2a). Nevertheless, the MTase domains of METTL3 and METTL14 lack an additional element similar to the target recognition domain (TRD) of DNA N^6-adenine MTase, which functions as the substrate-binding scaffold[8]. Consistent with the 22% sequence identity between the MTase domains of METTL3 and METTL14 (Extended Data Fig. 1), the structures of the two domains were superimposed with a root-mean-squared deviation (r.m.s.d.) of approximately 0.71 Å over 211 Cα atoms, excluding the NHM and CTM domains (Extended Data Fig. 2b). Interestingly, three loops with lower sequence similarities exhibited distinct conformations (Extended Data Figs 1, 2b), suggesting that they have different functions. We refer to these loops as gate loop 1 (residues 396–410 in METTL3), interface loop (residues 462–479 in METTL3) and gate loop 2 (residues 507–515 in METTL3; Fig. 1c).

METTL3 and METTL14 adopt the conformation of a tight asymmetric heterodimer with an interface area of approximately 2,500 Å² and engage in extensive water-mediated hydrogen-bond interactions with each other. These interactions are mediated by interfaces 1 and 2 (Extended Data Fig. 3a). Interface 1 primarily comprises the interface loop (residues 462–479) of METTL3, NHM, and the long loop connecting β5 and β6 of METTL14 (Extended Data Fig. 3b, left and middle). Additionally, R471 of METTL3 interacts with the C-terminal

[1]National Key Laboratory of Crop Genetic Improvement and National Centre of Plant Gene Research, Huazhong Agricultural University, Wuhan 430070, China. [2]Department of Pharmacology, Zhejiang University, School of Medicine, Hangzhou 310028, China. [3]CAS Key Laboratory of Magnetic Resonance in Biological Systems, State Key Laboratory of Magnetic Resonance and Atomic Molecular Physics, National Center for Magnetic Resonance at Wuhan, Wuhan Institute of Physics and Mathematics of the Chinese Academy of Sciences, Wuhan 430071, China. [4]College of Life Sciences and Technology, Huazhong Agricultural University, Wuhan 430070, China.
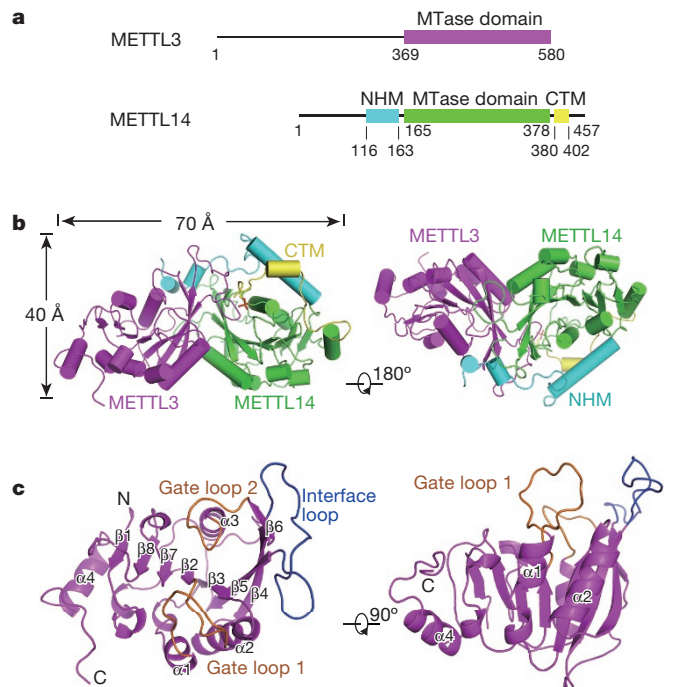*These authors contributed equally to this work.

Figure 1 | Structural overview of the METTL3–METTL14 complex.
a, Schematic domain structures of METTL3 and METTL14. METTL3 MTase (residues 369–580), METTL14 NHM (residues 116–163), MTase domain (residues 165–378), and CTM (residues 380–402) are magenta, cyan, green, and yellow, respectively. **b**, Overall structure of the METTL3–METTL14 heterodimer. Residue S399 (red stick) represents the phosphorylation modification. **c**, The METTL3 (magenta) structure in two perpendicular views. Gate loops 1 and 2 are orange, and the interface loop is blue. METTL14 has been removed for clarity. All structure figures were prepared using PyMOL.

Figure 2 | AdoMet is coordinated by METTL3 in the binary complex.
a, Ribbon representation of METTL3–METTL14 in complex with AdoMet. The bound AdoMet is illustrated as a green ball-and-stick representation. The DPPW motif is shown as an orange stick surrounded by a dashed line. **b**, Close-up view of the AdoMet binding site and DPPW motif of METTL3 showing the electron density (blue) of AdoMet contoured at 1σ. **c**, Schematic representation of the interactions between METTL3 and AdoMet. Residues are shown with sticks. The side-chain interactions and the main-chain interactions are shown in black and blue letters, respectively. Water is shown as a red ball representation. AdoMet is shown as green sticks. Hydrogen bonds are represented as red dashed lines.

phosphorylated S399 of METTL14 via a salt bridge, confirming the important regulatory role of phosphorylation. Interface 2 contains helix α2 (residues 438–447) and strand β4 (residues 450–460) of METTL3 and the corresponding helix α2, strand β4 and an interface loop (residues 266–284) from METTL14 (Extended Data Fig. 3b, right). These interfaces allow the two MTases to bind each other tightly, and the extensive interaction networks are difficult to disrupt.

After extensive trials, we determined the structure of METTL3–METTL14 in complex with AdoMet using a soaking approach and refined the structure to 1.71 Å resolution (Extended Data Table 1). In the crystal, one METTL3–METTL14 heterodimer was present in each asymmetric unit (Fig. 2a). Following assignment of most amino acids into the electron density map, electron densities indicative of one AdoMet became clearly visible in METTL3 (Fig. 2b), whereas no additional electron density was observed in METTL14 (Extended Data Fig. 4). The AdoMet molecule is positioned at the end of β1, β7 and β8 (Fig. 2a). The AdoMet-binding site faces the most conserved DPPW motif (residues 395–399) of gate loop 1 (Fig. 2a, b). This orientation suggests a nucleophilic attack methyl-transfer mechanism, reminiscent of the DNA N^6-adenine MTase[10].

The AdoMet molecule is primarily coordinated by eleven residues of METTL3 via extensive hydrogen bonds (Fig. 2c). The adenine moiety of AdoMet is recognized by the side chain of D377 and the main chain of I378. The hydroxyl groups of ribose are surrounded by Q550, N549 and R536. Several residues, including D395, K513, H538 and N539, contact the methionine moiety of AdoMet directly, while E532 and L533 form water-mediated interactions with AdoMet (Fig. 2c). The importance of these residues in AdoMet coordination is supported by mutational analysis. D377A, D395A, N539A and E532A mutations completely abolished enzyme activity, while substitutions of R536, H538, N549 or Q550 with alanine moderately reduced enzyme activity
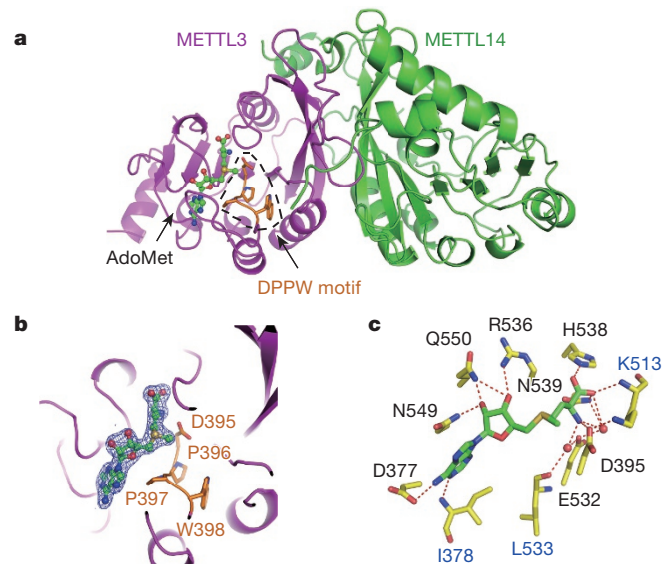
(Extended Data Fig. 5a). Neither the D377A nor the D395A mutant had detectable AdoMet-binding activity, as measured by isothermal titration calorimetry (ITC), compared to the wild-type complex, which exhibited a dissociation constant of approximately 1.5 μM and binding stoichiometry (N) of approximately 1.15 (Extended Data Fig. 5b, c).

Analysis of the surface electrostatic potential of the AdoMet-bound complex revealed a positively charged groove between METTL3 and METTL14 adjacent to the AdoMet (Fig. 3a). This groove consists of at least ten positively charged residues: R465, R471, H474 and H478 from the interface loop of METTL3 and R245, R249, R254, R255, K297 and R298 from METTL14 (Fig. 3b). We speculated that this groove might be responsible for RNA binding. To test this hypothesis, we first replaced the interface loop (residues 462–479) of METTL3 with six alanine amino acids. Compared to the wild-type complex, this mutant exhibited weaker RNA binding activity and reduced MTase activity, but no effect on AdoMet binding was observed (Fig. 3c and Extended Data Fig. 6a, b). A similar result was obtained when the positively charged residues in METTL14 were mutated (Fig. 3c and Extended Data Fig. 6). These results suggest that the positively charged groove formed by METTL3 and METTL14 contributes to internal RNA binding.

The 1.61 Å structure of METTL3–METTL14 in complex with AdoHcy was also determined (Extended Data Table 1). In this structure, one AdoHcy molecule is positioned in the AdoMet-binding pocket of METTL3. AdoHcy adopts a configuration nearly identical to that of AdoMet, except for the ribose (Extended Data Fig. 7a, b). The overall structures of the ligand-free, AdoMet-bound and AdoHcy-bound METTL3–METTL14 complexes are nearly identical, with an r.m.s.d. of 0.24 Å over 438 Cα atoms (ligand-free with AdoMet-bound) and 0.12 Å over 454 Cα atoms (AdoHcy-bound with AdoMet-bound; Fig. 4a). The structural similarities between the ligand-free and ligand-bound METTL3–METTL14 complexes were also confirmed by small-angle X-ray scattering measurements in solution (Extended Data Fig. 7c).
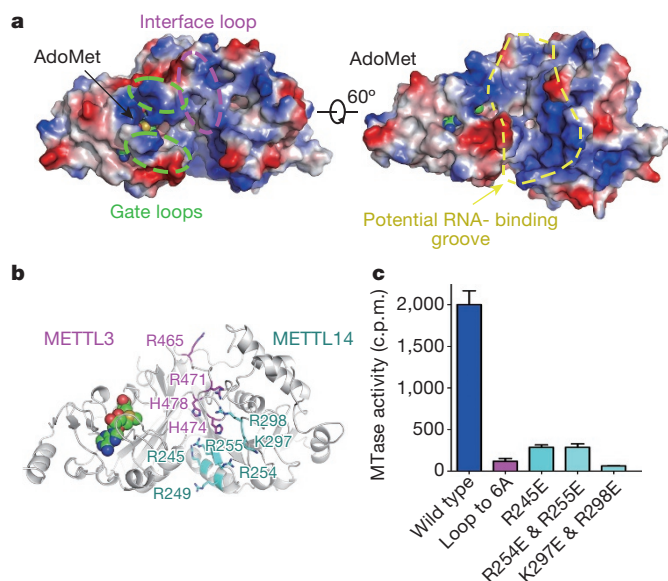
Figure 3 | Potential RNA-binding groove in the METTL3–METTL14 complex. a, Two views of the surface electrostatic potential calculated with PyMOL. The gate loops and the interface loop of METTL3 are highlighted by green dashed ellipses and a magenta dashed ellipse, respectively (left). The potential RNA-binding grove is encircled by a yellow dashed line (right). **b**, AdoMet in a space-filling representation. Residues from METTL3 and METTL14 are magenta and cyan, respectively. **c**, Measurement of the MTase activity of mutants of the putative RNA-binding groove of the METTL3–METTL14 complex. The indicated mutations were introduced to METTL3 (Loop to 6A) or METTL14 (R245E, R254E & R255E, K297E & R298E). The error bars represent the s.e.m. of three independent measurements.

Close inspection of the structures revealed that gate loop 1 and gate loop 2, which are adjacent to the AdoMet binding site, displayed large conformational changes upon ligand binding (Fig. 4a, b). Gate loop 1 is flipped outwards in the AdoMet-bound state compared with the AdoHcy-bound state, and the ligand-free state adopts the same fold as the AdoHcy-bound state (Fig. 4b). Likewise, gate loop 2 undergoes a significant conformational rearrangement upon binding of AdoHcy or AdoMet, resulting in closure of the binding pocket (Fig. 4a, b). This rearrangement is reminiscent of the interaction of loops 1 and 2 of M.TaqI with its DNA substrate (Extended Data Fig. 8a) and suggests that gate loops 1 and 2 have important roles in adenosine recognition[10].

The METTL3–METTL14 complex displayed much higher catalytic activity than either METTL3 or METTL14 alone (Extended Data Fig. 5a). This result suggests that METTL14 enhances the MTase activity of METTL3 via RNA binding, vice versa, or both. Our structures suggest that the primary function of METTL14 is not to catalyse methyl-group transfer but to offer an RNA-binding scaffold (Fig. 4c), similar to the TRD of DNA MTases[8-10] (Extended Data Fig. 8a, b). No positively charged area was observed near the potential AdoMet-binding pocket of METTL14 (Extended Data Fig. 8c). Most importantly, although most of the residues involved in AdoMet binding are conserved between METTL3 and METTL14 (Extended Data Figs 1, 8d), mutations of two key residues in METTL14 had little effect on the AdoMet-binding and MTase activities of the binary complex (Extended Data Fig. 8e, f). Consistent with this result, AdoMet was observed in only the METTL3 pocket in the crystal structure (Fig. 2). Nevertheless, we cannot exclude the possibility that METTL14 possesses MTase activity under certain conditions.

A recent study identified a METTL3 protein interaction network comprising additional components such as METTL14, WTAP and KIAA1429 (refs 7, 16, 26). Perturbation of these factors alters global m[6]A levels, resulting in epitranscriptomic changes[4,5]. Additionally,
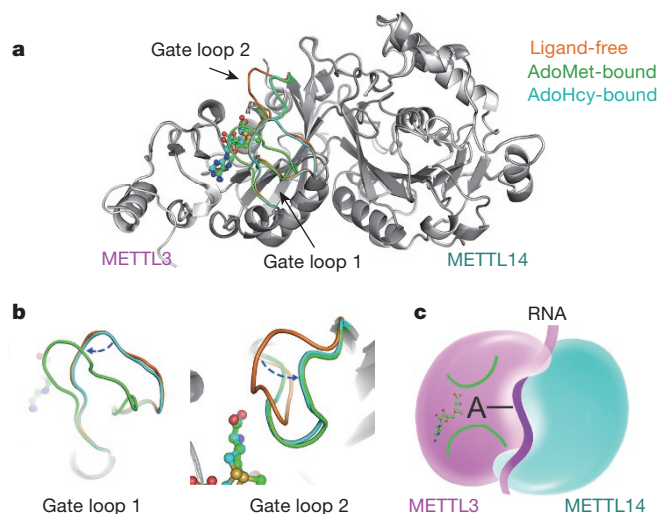

Figure 4 | Proposed working model of the METTL3–METTL14 complex. a, Structural superimposition of the ligand-free (orange), AdoMet-bound (green) and AdoHcy-bound (cyan) METTL3–METTL14 complexes shows the conformational changes in gate loops 1 and 2. AdoMet is show as green balls-and-sticks. **b**, Close-up view of gate loops 1 and 2. The conformational change is highlighted with a blue dashed arrow. **c**, Proposed working model for m[6]A modification by the METTL3–METTL14 complex. METTL3 (magenta) primarily functions as a catalytic core, and METTL14 (cyan) serves as an RNA-binding scaffold. The substrate RNA (magenta ribbon) is cooperatively coordinated by METTL3 and METTL14. The adenine base (black) points to the AdoMet binding site in METTL3 surrounded by the two gate loops (green).

the complex exhibited a substrate sequence preference (Extended Data Fig. 9). Further biochemical and structural characterization of the m[6]A writer complex containing regulatory factors, substrate RNA or both is required to completely elucidate the molecular basis of m[6]A modification. The structures reported here provide unprecedented mechanistic insight into m[6]A RNA methylation and new opportunities for the development of therapeutic agents, and serve as an important foundation for understanding m[6]A epitranscriptomics.

Online Content Methods, along with any additional Extended Data display items and Source Data, are available in the online version of the paper; references unique to these sections appear only in the online paper.

1. Lee, M., Kim, B. & Kim, V. N. Emerging roles of RNA modification: m[6]A and U-tail. *Cell* **158,** 980–987 (2014).
2. Meyer, K. D. & Jaffrey, S. R. The dynamic epitranscriptome: N[6]-methyladenosine and gene expression control. *Nature Rev. Mol. Cell Biol.* **15,** 313–326 (2014).
3. Fu, Y., Dominissini, D., Rechavi, G. & He, C. Gene expression regulation mediated through reversible m[6]A RNA methylation. *Nature Rev. Genet.* **15,** 293–306 (2014).
4. Schwartz, S. Cracking the epitranscriptome. *RNA* **22,** 169–174 (2016).
5. Liu, N. & Pan, T. N-methyladenosine-encoded epitranscriptomics. *Nature Struct. Mol. Biol.* **23,** 98–102 (2016).
6. Wang, Y. *et al.* N[6]-methyladenosine modification destabilizes developmental regulators in embryonic stem cells. *Nature Cell Biol.* **16,** 191–198 (2014).
7. Liu, J. *et al.* A METTL3–METTL14 complex mediates mammalian nuclear RNA N[6]-adenosine methylation. *Nature Chem. Biol.* **10,** 93–95 (2014).
8. Malone, T., Blumenthal, R. M. & Cheng, X. Structure-guided analysis reveals nine sequence motifs conserved among DNA amino-methyltransferases, and suggests a catalytic mechanism for these enzymes. *J. Mol. Biol.* **253,** 618–632 (1995).
9. Gupta, Y. K., Chan, S. H., Xu, S. Y. & Aggarwal, A. K. Structural basis of asymmetric DNA methylation and ATP-triggered long-range diffusion by EcoP15I. *Nat. Commun.* **6,** 7363 (2015).
10. Goedecke, K., Pignot, M., Goody, R. S., Scheidig, A. J. & Weinhold, E. Structure of the N[6]-adenine DNA methyltransferase M.TaqI in complex with DNA and a cofactor analog. *Nature Struct. Biol.* **8,** 121–125 (2001).
11. Deng, X. *et al.* Widespread occurrence of N[6]-methyladenosine in bacterial mRNA. *Nucleic Acids Res.* **43,** 6557–6567 (2015).

12. Schwartz, S. *et al.* High-resolution mapping reveals a conserved, widespread, dynamic mRNA methylation program in yeast meiosis. *Cell* **155**, 1409–1421 (2013).
13. Luo, G. Z. *et al.* Unique features of the m6A methylome in *Arabidopsis thaliana*. *Nat. Commun.* **5**, 5630 (2014).
14. Meyer, K. D. *et al.* Comprehensive analysis of mRNA methylation reveals enrichment in 3′ UTRs and near stop codons. *Cell* **149**, 1635–1646 (2012).
15. Dominissini, D. *et al.* Topology of the human and mouse m6A RNA methylomes revealed by m6A-seq. *Nature* **485**, 201–206 (2012).
16. Ping, X. L. *et al.* Mammalian WTAP is a regulatory subunit of the RNA N^6-methyladenosine methyltransferase. *Cell Res.* **24**, 177–189 (2014).
17. Fustin, J. M. *et al.* RNA-methylation-dependent RNA processing controls the speed of the circadian clock. *Cell* **155**, 793–806 (2013).
18. Geula, S. *et al.* Stem cells. m6A mRNA methylation facilitates resolution of naive pluripotency toward differentiation. *Science* **347**, 1002–1006 (2015).
19. Chen, T. *et al.* m6A RNA methylation is regulated by microRNAs and promotes reprogramming to pluripotency. *Cell Stem Cell* **16**, 289–301 (2015).
20. Zhou, J. *et al.* Dynamic m6A mRNA methylation directs translational control of heat shock response. *Nature* **526**, 591–594 (2015).
21. Liu, N. *et al.* N^6-methyladenosine-dependent RNA structural switches regulate RNA-protein interactions. *Nature* **518**, 560–564 (2015).
22. Wang, X. *et al.* N^6-methyladenosine modulates messenger RNA translation efficiency. *Cell* **161**, 1388–1399 (2015).
23. Choi, J. *et al.* N^6-methyladenosine in mRNA disrupts tRNA selection and translation-elongation dynamics. *Nature Struct. Mol. Biol.* **23**, 110–115 (2016).
24. Wang, X. *et al.* N^6-methyladenosine-dependent regulation of messenger RNA stability. *Nature* **505**, 117–120 (2014).
25. Alarcón, C. R., Lee, H., Goodarzi, H., Halberg, N. & Tavazoie, S. F. N^6-methyladenosine marks primary microRNAs for processing. *Nature* **519**, 482–485 (2015).
26. Schwartz, S. *et al.* Perturbation of m6A writers reveals two distinct classes of mRNA methylation at internal and 5′ sites. *Cell Rep.* **8**, 284–296 (2014).
27. Jia, G. *et al.* N^6-methyladenosine in nuclear RNA is a major substrate of the obesity-associated FTO. *Nature Chem. Biol.* **7**, 885–887 (2011).
28. Zheng, G. *et al.* ALKBH5 is a mammalian RNA demethylase that impacts RNA metabolism and mouse fertility. *Mol. Cell* **49**, 18–29 (2013).
29. Xiao, W. *et al.* Nuclear m6A reader YTHDC1 regulates mRNA splicing. *Mol. Cell* **61**, 507–519 (2016).
30. Iyer, L. M., Zhang, D. & Aravind, L. Adenine methylation in eukaryotes: Apprehending the complex evolutionary history and functional potential of an epigenetic modification. *Bioessays* **38**, 27–40 (2016).

METHODS

No statistical methods were used to predetermine sample size. The experiments were not randomized and the investigators were not blinded to allocation during experiments and outcome assessment.

METTL3 and METTL14 construction, expression and purification. The *METTL3* and *METTL14* genes were amplified from a *Homo sapiens* cDNA library using the following primer pairs: METTL3-M1-F (5′-ATGTCGGACACGTGGAGCT-3′) and M3ETTL3-L580-R (5′-CTATAAATTCTTAGGTTTAGAGATGATAC-3′); and METTL14-M1-F (5′-GATAGCCGCTTGCAGGAGATCCG-3′) and METTL14-R456-R (5′-TCGAGGTGGAAAGCCACCTCTG-3′), and cloned into the T-vector. Both gene strands were verified by sequencing. The full length of genes *METTL3* and *METTL14* was subcloned into a modified pFastBac1 vector with a His$_{10}$ affinity tag fused to the N terminus. Bacmids were generated in DH10Bac cells following the instructions for the Bac-to-Bac baculovirus expression system (Invitrogen), and baculoviruses were generated and amplified in Sf-9 insect cells. For protein expression and purification, High Five (*Trichoplusia ni*) insect cells were grown in SIM HF medium (Sino Biological Inc.) supplemented with L-glutamine. The METTL3–METTL14 complex was co-expressed in High Five insect cells at 27 °C for 72 h using the METTL3 and METTL14 viruses. All complex mutants were co-expressed using a mutant virus and a wild-type partner virus. Cells were harvested by centrifugation at 2,000g for 15 min and homogenized in ice-cold lysis buffer containing 25 mM Tris-HCl, pH 8.0, 150 mM NaCl and 0.5 mM phenyl-methanesulfonyl-fluoride (PMSF). The cells were disrupted using a cell homogenizer. The insoluble fraction was precipitated by ultracentrifugation (20,000g) for 1 h at 4 °C. The supernatant was loaded onto a Ni-NTA superflow affinity column (Qiagen) and washed three times with lysis buffer plus 10 mM imidazole. Elution was performed in buffer containing 25 mM Tris-HCl, pH 8.0, and 250 mM imidazole. The protein was further purified using anion-exchange chromatography (Source 15Q, GE Healthcare). The purified complex was concentrated to approximately 20 mg ml^{-1} (Amicon 30-kDa cutoff, Millipore), and if for crystallization, it was digested with chymotrypsin (0.5 mg ml^{-1}) at room temperature for 30 min. The undigested or digested protein was subjected to size-exclusion chromatography (Superdex-200 Increase 10/300, GE Healthcare). The buffer used for size-exclusion chromatography contained 25 mM Tris-HCl, pH 8.0, 150 mM NaCl and 5 mM dithiothreitol (DTT). The peak fractions of the METTL3–METTL14 complex were pooled and immediately used for crystallization.

Crystallization. Crystallization experiments were performed using the sitting-drop vapour diffusion method at 18 °C by mixing equal volumes (1 µl) of protein (15 mg ml^{-1}) and reservoir solution. After several rounds of optimization, good-quality crystals appeared after several days and grew as a thin diamond to full size within 15 days in drops containing 18% (v/v) PEG 8000 (Sigma) and 0.1 M sodium citrate, pH 5.7. The crystals were flash-frozen in liquid nitrogen and cryoprotected by adding ethylene glycol to a final concentration of 20%. The crystals were diffracted to 1.9 Å at the Shanghai Synchrotron Radiation Facility on beamlines BL17U and BL19U. To obtain phase information, high-quality crystals were immersed in cryoprotectant solution plus 0.3 M NaBr for 10 min. Before the crystals were harvested, 1 µl of a solution containing 25 mM Tris, pH 8.0, 150 mM NaCl, 20% (v/v) ethylene glycol and 0.1 M NaBr was added. The crystals were immediately transferred to a new solution containing 25 mM Tris, pH 8.0, 150 mM NaCl, ~18% (v/v) ethylene glycol and 0.3 M NaBr. Finally, the bromide-soaked crystals were diffracted to 2.6 Å resolution.

To obtain the AdoMet-bound and AdoHcy-bound structures, we performed extensive trials. We initially failed to obtain diffracting crystals by co-crystallization of METTL3–METTL14 with ligand. We then systematically soaked high-quality diffracting crystals of METTL3–METTL14 with AdoMet or AdoHcy (Sigma). Native crystals of METTL3–METTL14 were obtained after at least 15 days of incubation at 18 °C. The crystals were soaked with a series of ligand concentrations in the presence of 3 mM ATP as an additive. The final concentrations of ligand used were 0.5, 1, 2 and 5 mM. The crystals were soaked for 30 min to 72 h, depending on their survival in the soaking solution. The crystals were examined under a microscope every 30 min. If the crystals appeared damaged, they were transferred to a cryoprotectant solution containing 25 mM Tris pH 8.0, 150 mM NaCl and 18% (v/v) ethylene glycol. The crystals were collected and immediately flash-frozen in liquid nitrogen.

Data collection and structure determination. All diffraction data were collected at the Shanghai Synchrotron Radiation Facility (SSRF) on beamlines BL17U or BL19U using a CCD detector cooled to 100 K. The data from the METTL3–METTL14 crystals were processed with the HKL2000 program suite and XDS packages[31]. Further processing was performed using the programs from the CCP4 suite[32]. The ligand-free METTL3–METTL14 structure was solved via single anomalous diffraction (SAD) of bromide using the ShelxC/D/E program[33]. Then, a crude model was manually built in the Coot program[34]. The $P4_12_12$ crystal forms of the

AdoMet-bound and AdoHcy-bound complexes were solved by molecular replacement with PHASER using the structure of the ligand-free METTL3–METTL14 complex as the initial searching model[35]. All four crystal structures were built using Coot and refined using the Phenix program[36]. The data collection and structure refinement statistics are summarized in Extended Data Table 1. All figures representing structures were prepared with PyMOL[37].

m^{6}A methylation assay. A 5′-GG$\underline{A}$CUGG$\underline{A}$CUGG$\underline{A}$CUGG$\underline{A}$CU-3′ RNA probe containing four repeats of the canonical RRACH sequence was synthesized *in vitro* (Takara). Before reaction, the proteins were subjected to size-exclusion chromatography (Superdex-200 Increase 10/300, GE Healthcare) and the running buffer contains 15 mM HEPES pH 7.3, 150 mM NaCl, 5 mM MgCl$_2$, and 5 mM dithiothreitol (DTT). The 50-µl reaction mixture contained 15 mM HEPES pH 7.3, 50 mM KCl, 50 mM NaCl, 1 mM MgCl$_2$, 1 mM dithiothreitol, 4% glycerol, 0.04 µCi [methyl-^{3}H]AdoMet (PerkinElmer), 2 nM RNA probe, and 250 ng purified protein. The solution was incubated at 30 °C for 1 h. A 5′-GG$\underline{G}$CUGG$\underline{G}$CUGG$\underline{G}$CUGG$\underline{G}$CU-3′ RNA probe without adenine was used as a negative control. This reaction was quenched with 500 µl of 1:1 (v/v) Tris-phenol (pH 8.0):chloroform, followed by the addition of 450 µl double-distilled (dd)H$_2$O. Then, the solution was centrifuged at 20,000g for 15 min. The supernatant was removed to a new tube and precipitated using an equal volume of isopropanol and 50 µg yeast tRNA at −20 °C for 1 h. The precipitated RNA was dissolved in 100 µl ddH$_2$O. The products were confirmed by immunoblotting using the commercial m^{6}A antibody (Synaptic Systems, catalogue number 202 003, 1:3,000). The counts per minute (c.p.m.) of the RNA was measured in a scintillation counter (1450 MicroBeta Trilux, PerkinElmer). All experiments were repeated three times for each measurement. The average (±s.e.m.) c.p.m. was determined from three independent experiments.

Isothermal titration calorimetry (ITC) assays. ITC experiments for the binding of AdoMet to the METTL3–METTL14 complex were performed at 25 °C using Auto-iTC100 titration calorimetry (MicroCal). AdoMet (200 µM) was dissolved in reaction buffer containing 20 mM Tris-HCl, pH 8.0, and 150 mM NaCl (40 µl) and titrated against 20 µM wild-type or mutant METTL3–METTL14 complex (200 µl) in the same buffer. The first injection (0.5 µl) was followed by 19 injections of 2 µl. The heat of dilution values for AdoMet were measured by injecting AdoMet into buffer alone. The values were subtracted from the experimental curves before data analysis. The stirring rate was 750 r.p.m. The MicroCal ORIGIN software supplied with the instrument was used to determine the site-binding model that produced a good fit (low × 2 value) for the resulting data.

Electrophoretic mobility shift assay (EMSA). The ssRNA oligonucleotide 5′-GGACUGGACUGGACUGGACU-3′ was radiolabelled at the 5′ end with [γ-^{32}P]ATP (PerkinElmer), catalysed by T4 polynucleotide kinase (Takara). In addition, the RNA was purified by centrifugation through a 2-cm bed of G-25 size exclusion resin packed in a mini-spin column (GE Healthcare) and centrifuged at 750g for 2 min. For EMSA, proteins were incubated with approximately 10 nM ^{32}P-labelled probe in final binding reactions containing 20 mM HEPES, pH 7.0, 5 mM MgCl$_2$, 40 mM NaCl, 1.5 µM yeast tRNA and 10% glycerol for 20 min at 25 °C. The reactions were then resolved on 6% native acrylamide gels (37.5:1 acrylamide:bis-acrylamide) in 0.5 × Tris-glycine buffer under an electric field of 15 V cm^{-1} for 1 h. Gels were visualized on a phosphor screen (Amersham Biosciences) using a Typhoon Trio Imager (Amersham Biosciences).

Small-angle X-ray scattering (SAXS) measurement. Solution SAXS data were collected at the National Center for Protein Science Shanghai using the BL19U2 beamline at 18 °C. The complex proteins for SAXS measurement were prepared at 30 µM in buffer containing 25 mM HEPES, pH 7.0, 150 mM NaCl without ligand or in the presence of equimolar AdoMe or AdoHcy. For each measurement, 20 consecutive frames of 1-s exposure time were recorded and were averaged after checking there was no difference between the first and last frames of the SAXS data. Similarly, the background data were recorded using the sample buffer and were subtracted from the protein patterns.

31. Otwinowski, Z. & Minor, W. Processing of X-ray diffraction data collected in oscillation mode. *Methods Enzymol.* **276,** 307–326 (1997).
32. Collaborative Computational Project The CCP4 suite: programs for protein crystallography. *Acta Crystallogr. D* **50,** 760–763 (1994).
33. Schneider, T. R. & Sheldrick, G. M. Substructure solution with SHELXD. *Acta Crystallogr. D* **58,** 1772–1779 (2002).
34. Emsley, P. & Cowtan, K. Coot: model-building tools for molecular graphics. *Acta Crystallogr. D* **60,** 2126–2132 (2004).
35. McCoy, A. J. *et al.* Phaser crystallographic software. *J. Appl. Crystallogr.* **40,** 658–674 (2007).
36. Adams, P. D. *et al.* PHENIX: building new software for automated crystallographic structure determination. *Acta Crystallogr. D* **58,** 1948–1954 (2002).
37. DeLano, W. L. The PyMOL molecular graphics system. http://www.pymol.org (2002).
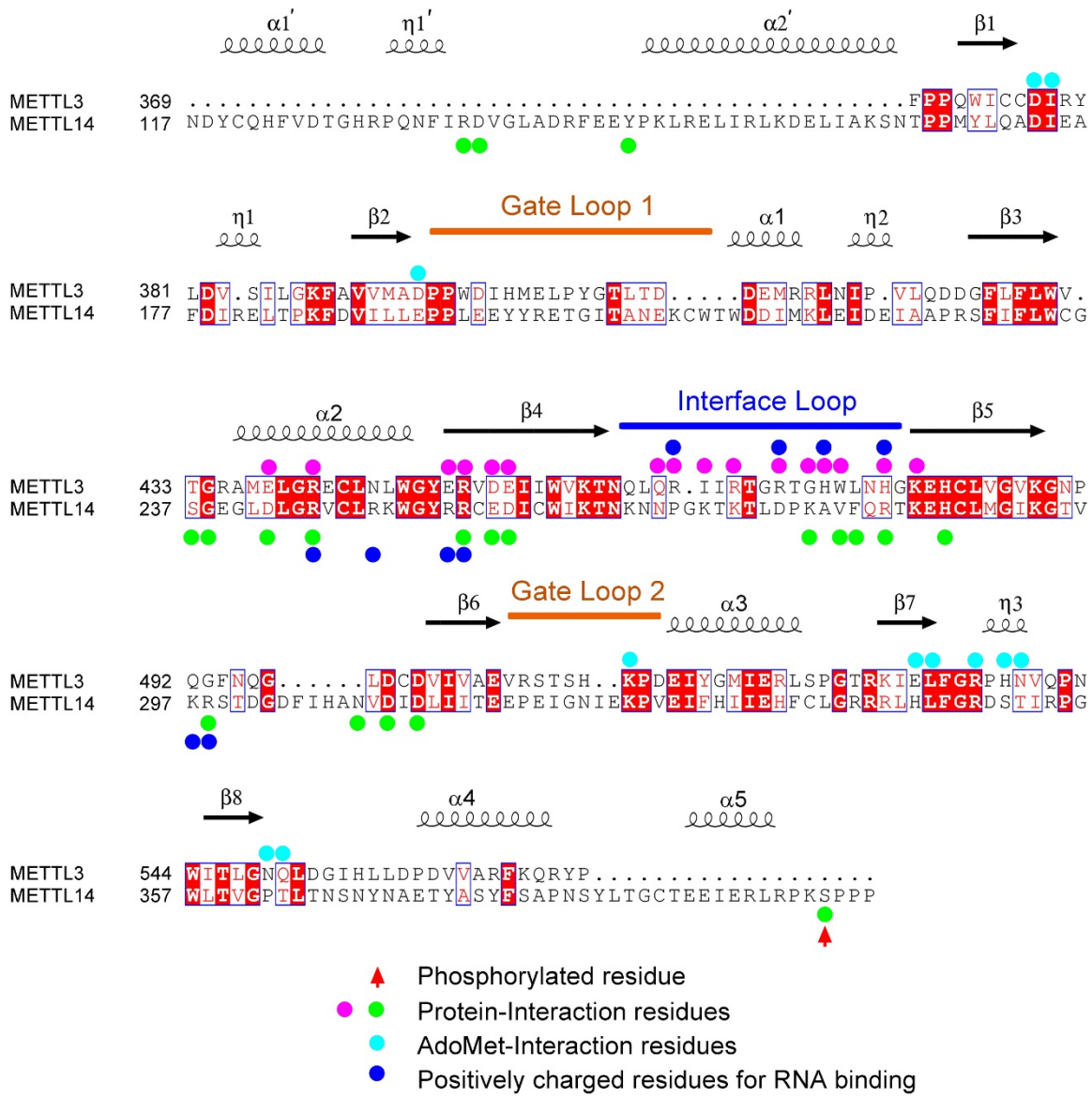
Extended Data Figure 1 | Sequence alignment of human METTL3 and METTL14. Sequence alignment of *Homo sapiens* METTL3 (UniProt accession Q86U44) and METTL14 (UniProt accession Q9HCE5). The alignment was generated using the MultAlin and ENDscript programs. Secondary structural elements are shown above. Sequence identity is shown in white letters with a red background, and sequence similarity is shown in red letters. The coloured dots highlight functionally important positions. Residues of METTL3 and METTL14 that are involved in protein interactions are indicated by magenta and green dots, respectively. Cyan dots indicate residues that interact with AdoMet that were analysed by mutagenesis in this study. Blue dots represent residues that compose the RNA binding groove. The dots at the top and bottom of the sequences indicate residues from METTL3 and METTL14, respectively. Phosphoserine is highlighted by a red arrow.

a
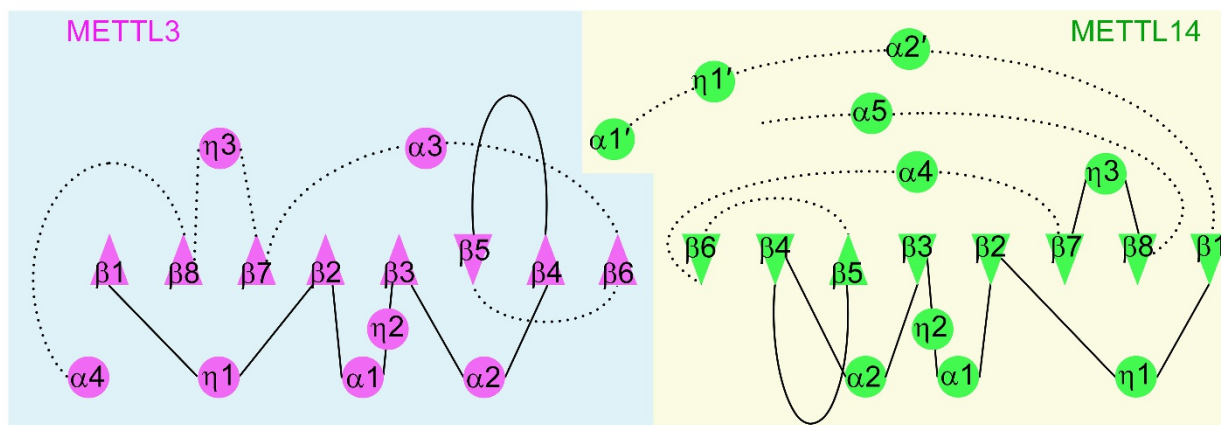
b
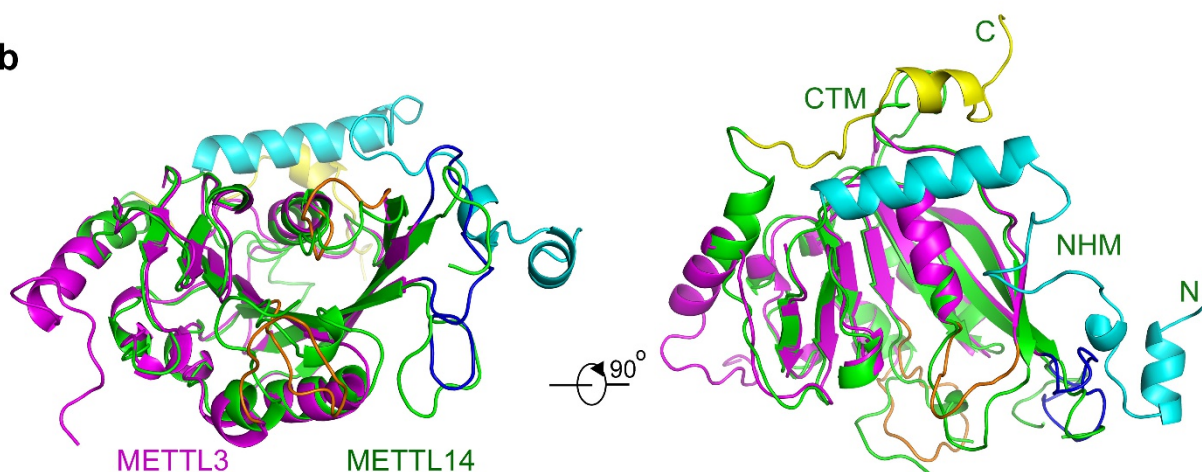
Extended Data Figure 2 | The MTase domains of METTL3 and METTL14 adopt the class I MTase fold. a, Diagram of the METTL3–METTL14 secondary structure profiles. METTL3 (magenta) and METTL14 (green) are boxed with a light teal background and a wheat background, respectively. The MTase domain contains an eight-stranded β-sheet (triangles) flanked by four α-helices and three 3_{10}-helices (circles). Structural elements are numbered by their linear order in the sequence. The loops in the front are indicated by black lines, and loops in the back are indicated by black dashed lines. **b**, Structural comparison of METTL3 and METTL14. Two perpendicular views of superimposed METTL3 and METTL14 coloured magenta and green, respectively. The NHM and CTM of METTL14 are coloured cyan and yellow, respectively. The main differences between the MTase domains of METTL3 and METTL14 are the two gate loops (orange) and the interface loop (blue).
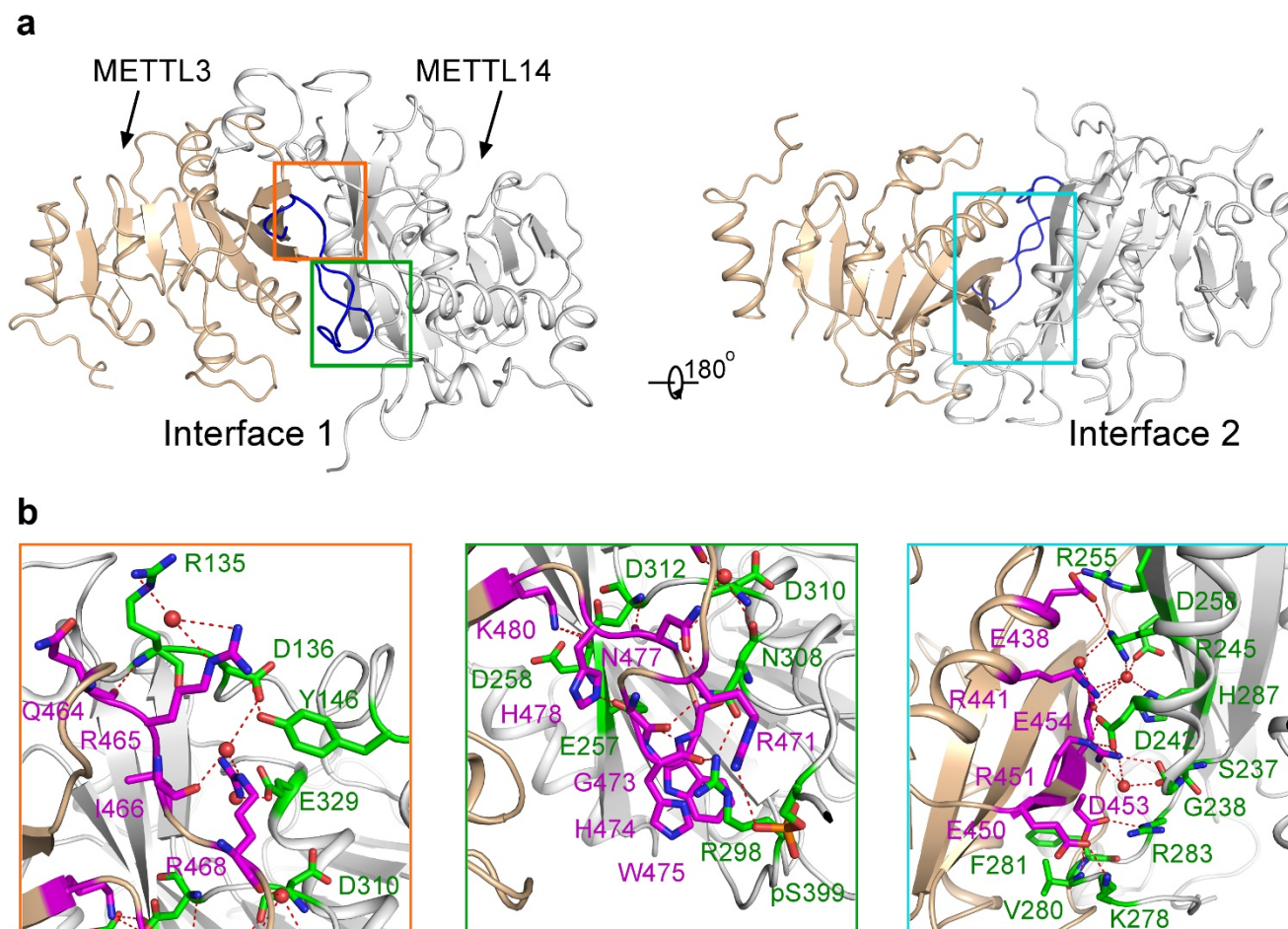
Extended Data Figure 3 | Extensive hydrogen network between METTL3 and METTL14. a, The main interface of the METTL3–METTL14 heterodimer comprises interface 1 (boxed with orange and green rectangles) and interface 2 (boxed with a cyan rectangle), which generate an extensive water-mediated hydrogen network. METTL3 and METTL14 are coloured wheat and silver, respectively. The interface loop of METTL3 (blue) primarily contributes to the heterodimer interaction. **b**, Details of interfaces 1 and 2. Water is shown as a red ball. Hydrogen bonds are represented by red dashed lines. Residues from METTL3 (magenta) and METTL14 (green) that are involved in interactions are shown as sticks.

a

METTL3   METTL14

b

c
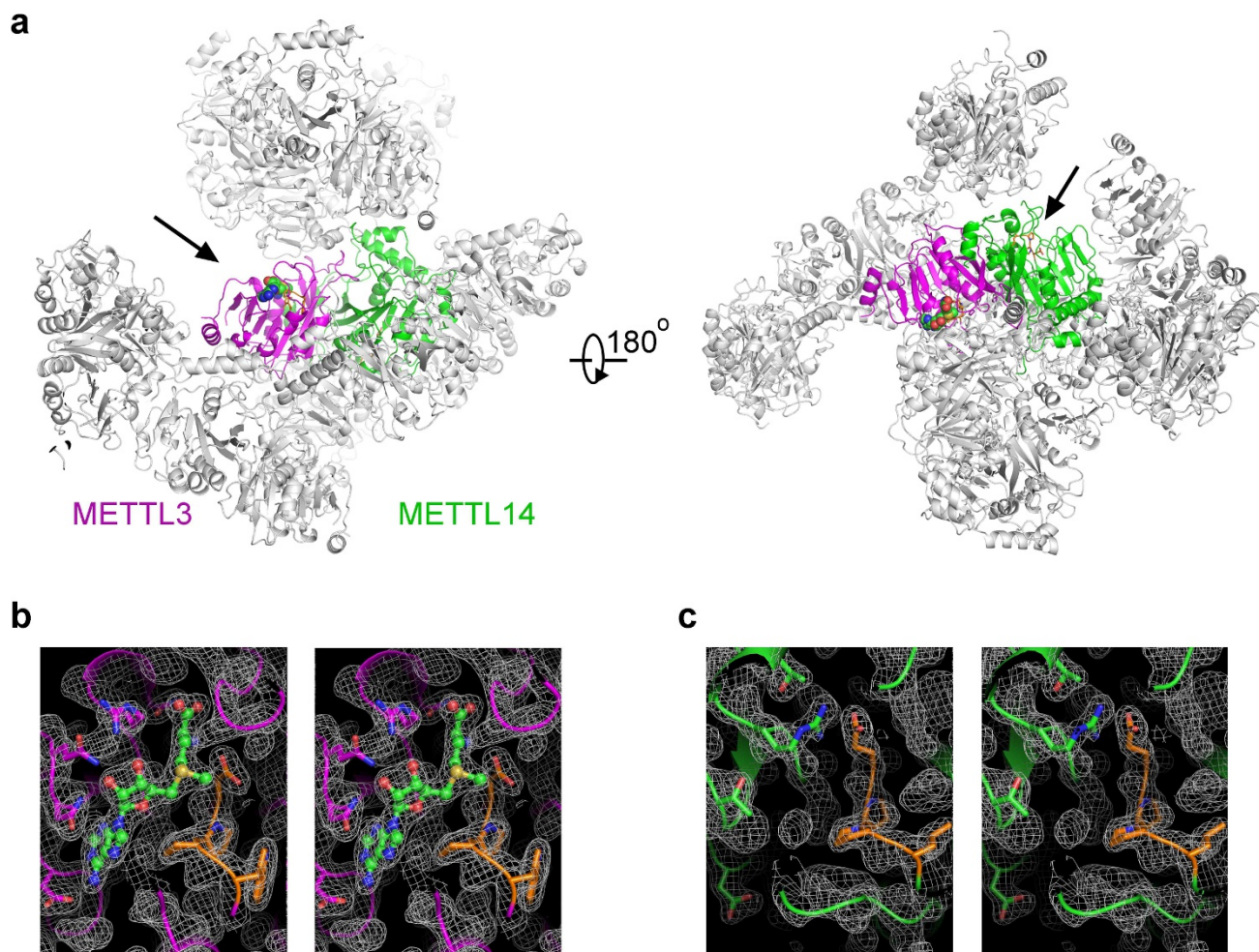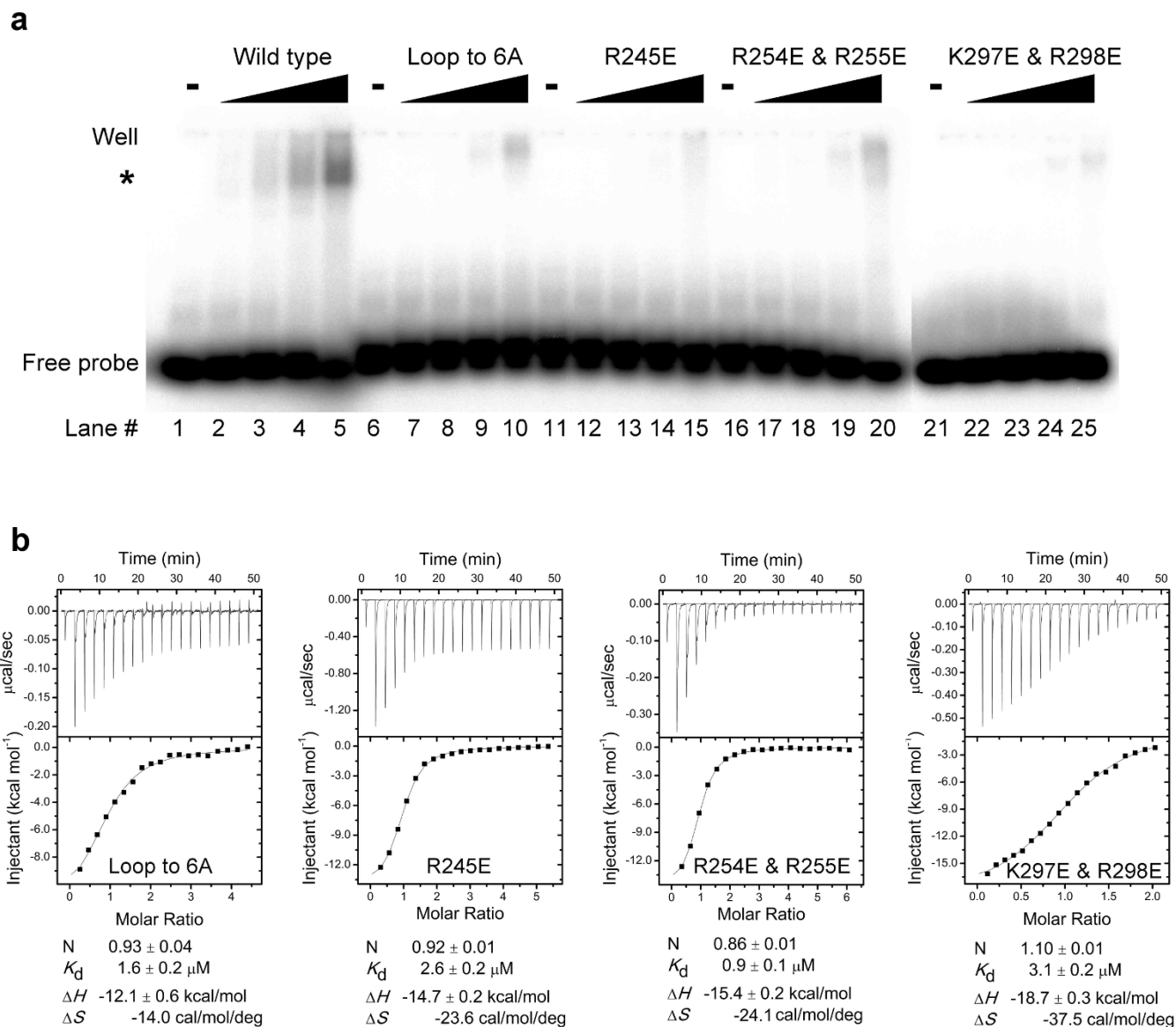

Extended Data Figure 4 | One AdoMet was located at the AdoMet binding site of METTL3. a, Lattice packing of AdoMet-bound complex. One AdoMet (green sphere) was coordinated by METTL3 (purple) but not METTL14 (green). The arrow shows the putative AdoMet-binding pocket. **b**, Stereo views of electron density map of AdoMet binding site of METTL3. $2F_o - F_c$ electron density (grey) of AdoMet binding site in METTL3, contoured at 1.0σ. AdoMet is show as green balls-and-sticks and surrounding residues in magenta with the DPPW motif (orange). **c**, Representative $2F_o - F_c$ electron density (grey) of AdoMet binding site in METTL14, contoured at 1.0σ. The electron density of METTL14 (grey) is clearly visible and the EPPL motif is coloured orange. No additional apparent electron density was observed in the putative AdoMet binding site of METTL14.

a

b

N 1.15 ± 0.02
K_d 1.5 ± 0.2 μM
ΔH -14.7 $\pm$ 0.4 kcal/mol
ΔS -22.6 cal/mol/deg

Wild Type

c

D377A

D395A
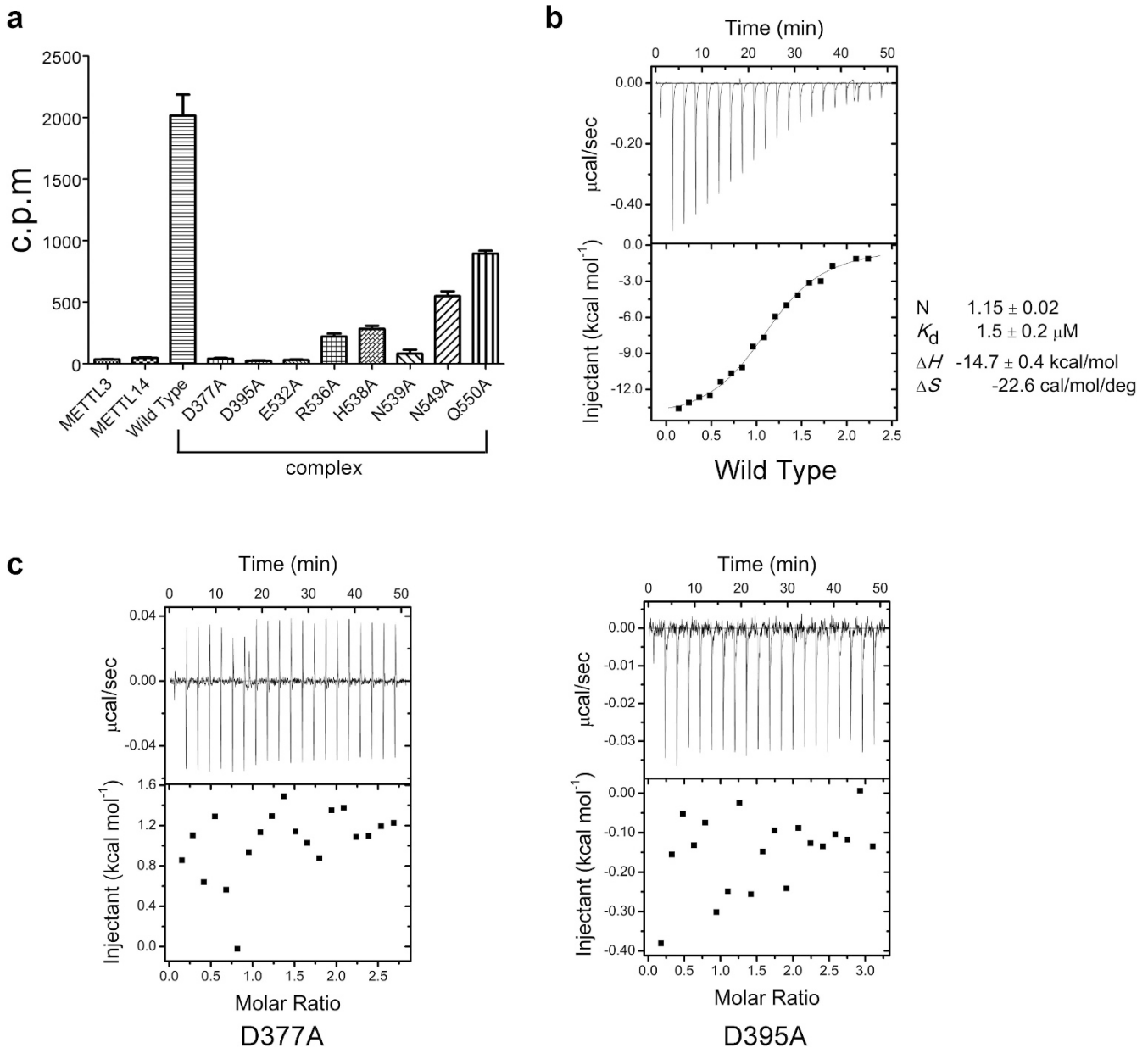
Extended Data Figure 5 | Mutagenesis analysis of the METTL3–METTL14–AdoMet interaction. a, Characterization of METTL3–METTL14 mutations affecting MTase activity. The indicated point mutations were introduced into METTL3. Each METTL3 mutant was co-expressed and purified with wild-type METTL14 as a binary complex and used for the MTase and ITC assays. Methylation yields were calculated based on the c.p.m. of the extracted tritium-labelled RNA probe. The c.p.m. of the extracted RNA was measured in a scintillation counter. The data are shown as mean $\pm$ s.e.m. from experiments that were independently repeated at least three times. All alanine substitutions resulted in remarkable decreases in activity. **b**, **c**, Measurement of the binding affinity between AdoMet and the METTL3–METTL14 complex (wild-type and D377A for METTL3 and D395A for METTL3) using ITC. Individual peaks from titrations were integrated and presented in a Wiseman plot. The first dot was removed from the analysis. The dissociation constant (K_d) and the binding stoichiometry (N) of the wild type were approximately 1.5 μM and 1.15, respectively. The mutants exhibited undetectable AdoMet binding activity.

a

b

|	Loop to 6A		R245E		R254E & R255E		K297E & R298E
N	0.93 ± 0.04	N	0.92 ± 0.01	N	0.86 ± 0.01	N	1.10 ± 0.01
K_d	1.6 ± 0.2 μM	K_d	2.6 ± 0.2 μM	K_d	0.9 ± 0.1 μM	K_d	3.1 ± 0.2 μM
ΔH	-12.1 ± 0.6 kcal/mol	ΔH	-14.7 ± 0.2 kcal/mol	ΔH	-15.4 ± 0.2 kcal/mol	ΔH	-18.7 ± 0.3 kcal/mol
ΔS	-14.0 cal/mol/deg	ΔS	-23.6 cal/mol/deg	ΔS	-24.1 cal/mol/deg	ΔS	-37.5 cal/mol/deg

Extended Data Figure 6 | Biochemical analysis of the role of the potential RNA binding groove. a, RNA binding activity of the METTL3–METTL14 complex revealed by EMSA. The final concentrations of proteins in each set of five lanes (1–5, 6–10, 11–15, 16–20 and 21–25) were 0, 0.19, 0.56, 1.67 and 5 μM, respectively. 'Well' indicates the top of native gel. The RNA-bound complex is highlighted by a black asterisk. The wild-type complex binds to the substrate RNA probe weakly (the dissociation constant is approximately 10 μM). All of the mutants showed moderately reduced RNA binding activity. These results suggested that the positively charged groove is involved in RNA interactions. For uncropped gels, see Supplementary Fig. 1. **b**, Measurement of the binding affinity between AdoMet and the METTL3–METTL14 complex mutants using ITC. These mutations in METTL3 or METTL14 had little effect on AdoMet binding activity.

a

b

c
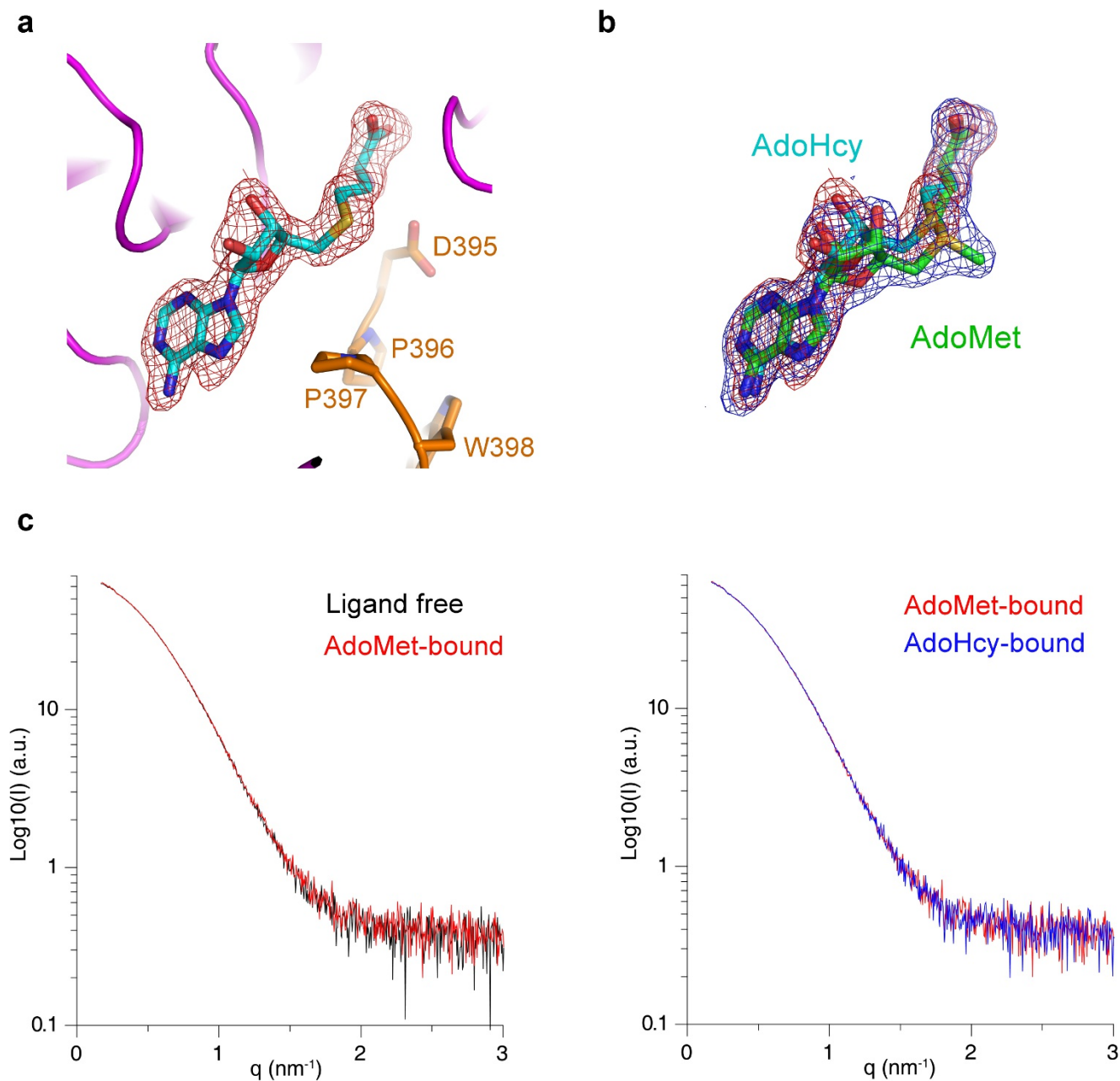
Extended Data Figure 7 | There is little conformational change in overall structure between the AdoMe-bound and AdoHcy-bound states.
a, Electron density maps of AdoHcy showing $2F_o − F_c$ electron density (red) of AdoHcy adjacent to the DPPW motif (orange) contoured at 1.0σ. The DPPW motif is shown as sticks. AdoHcy is shown as cyan sticks. **b**, Structural comparison of AdoHcy (cyan) and AdoMet (green); the electron densities are shown as red and blue meshes, respectively. AdoHcy and AdoMet exhibited nearly identical configurations except for ribose. **c**, SAXS measurements reveal little structural difference among the ligand-free, AdoMe-bound and AdoHcy-bound states. Superposition of the SAXS curves of ligand-free protein complex (black), and in the presence of AdoMet (red) or AdoHcy (blue).
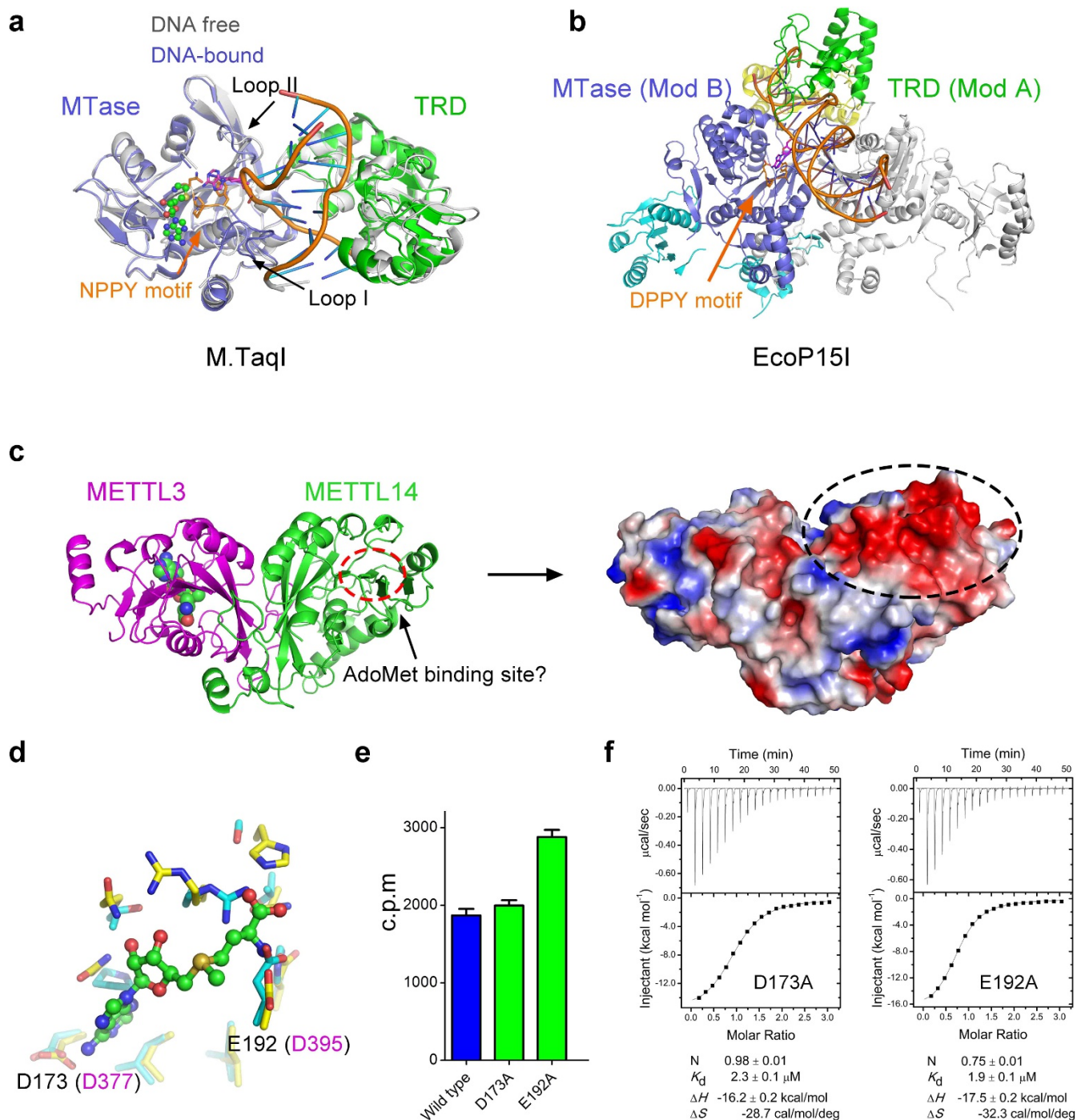
Extended Data Figure 8 | Potential role of METTL14. a, Structural comparison with the DNA-free (PDB: 2ADM) and DNA-bound (PDB: 1G38) states of M.TaqI. M.TaqI contains the target recognition domain (TRD, green), DNA (orange) and MTase domain (slate). The TRD functions as a scaffold for substrate DNA recognition, and the MTase domain functions as an enzyme. Adenine (magenta) is flipped out and points to the ligand-binding pocket. Black arrows highlight the loop conformational changes, which are similar to those of gate loops 1 and 2 in the METTL3–METTL14 complex. **b**, Ribbon representation of the DNA-bound state of EcoP15I (PDB: 4ZCF). The TRD (green) of ModA recognizes DNA, while the MTase (slate) of ModB methylates the target adenine. **c**, The putative AdoMet-binding site of METTL14 (green) is highlighted by a red dashed ellipse. AdoMet coordinated by METTL3 (magenta) is shown as a space-filling representation. The surface electrostatic potential around the putative AdoMet-binding site of METTL14 revealed a negative charge (black dashed ellipse) and suggests a dispensable role for this region in RNA binding. **d**, Most of the putative AdoMet-binding site residues were conserved between METTL3 (cyan) and METTL14 (yellow). **e**, Each complex containing alanine substitution mutants of residues in METTL14 (D173 and E192) that correspond to critical residues in METTL3 (D377 and D395) displayed similar methylation activity to the wild type. The average ($\pm$ s.e.m.) c.p.m. was determined from three independent experiments. **f**, The complex mutants exhibited similar AdoMet-binding activities to the wild-type complex.
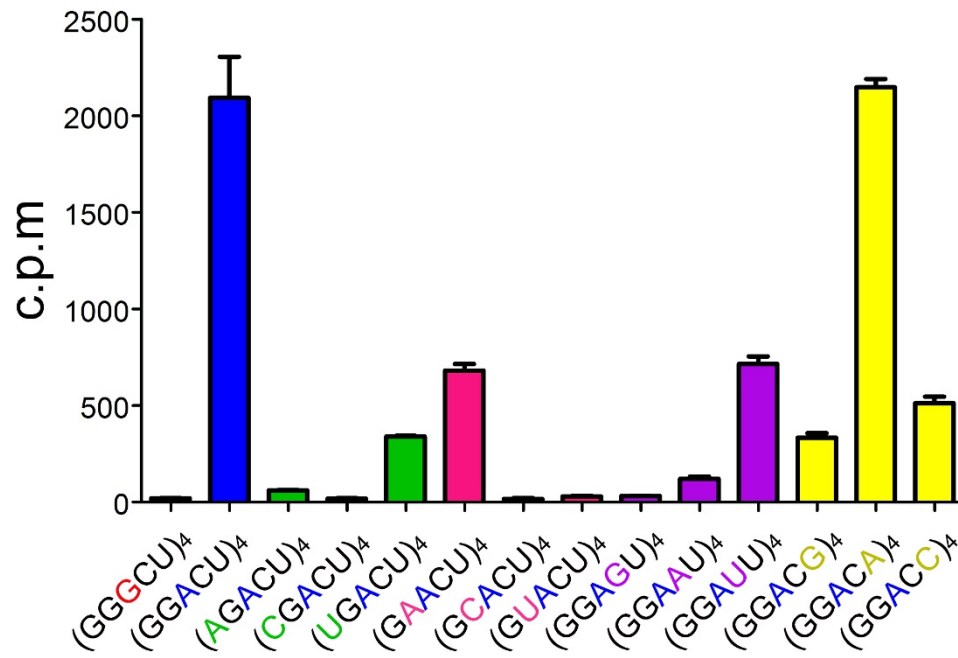
Extended Data Figure 9 | Substrate sequence preference of the METTL3–METTL14 complex. The 20-nucleotide RNA substrate contains four repeats of the consensus sequence GGACU. Each site was substituted by the other three kinds of nucleotide. The average ($\pm$ s.e.m.) c.p.m. was determined from three independent experiments.

Extended Data Table 1 | Data collection, phasing and refinement statistics

	Br-SAD	Ligand-free (5IL0)	AdoMet-bound (5IL1)	AdoHcy-bound (5IL2)
Data collection				
Space group	$P4_12_12$	$P4_12_12$	$P4_12_12$	$P4_12_12$
Cell dimensions				
a, b, c (Å)	101.77, 101.77, 116.59	101.70, 101.70, 116.48	102.34, 102.34, 116.72	101.87, 101.87, 115.84
α, β, γ (°)	90,90,90	90,90,90	90,90,90	90,90,90
Resolution (Å)	45~2.60 (2.69~2.60)	50~1.88 (1.95~1.88)	45~1.71 (1.74~1.71)	45~1.61 (1.63~1.61)
R_{merge}	8.2 (19.4)	11.4 (127.0)	7.6 (194.7)	6.5 (116.2)
$I/\sigma(I)$	70.1 (31.7)	37.5 (2.0)	17.7 (1.4)	21.3 (2.3)
Completeness (%)	100 (99.9)	99.9 (98.9)	100 (99.4)	99.9 (98.8)
Redundancy	30.4 (30.4)	14.3 (12.6)	13.2 (13.1)	13.2 (13.2)
Refinement				
No. reflections		50,070	67,756	79,742
R_{work}/R_{free}		17.68/20.77	17.98/20.69	18.48/19.92
No. atoms				
Protein		4015	3960	3975
Ligand/ion		9	39	42
Water		331	337	376
B-factors				
Protein		42.4	43.0	36.9
Ligand/ion		57.4	45.5	45.1
Water		43.1	44.2	42.0
R.m.s deviations				
Bond lengths (Å)		0.007	0.007	0.011
Bond angles (°)		0.874	0.904	1.311

Values in parentheses are for the highest-resolution shell.

CORRECTIONS & AMENDMENTS

Corrigendum: Structural basis of N^6–adenosine methylation by the METTL3–METTL14 complex

Xiang Wang, Jing Feng, Yuan Xue, Zeyuan Guan, Delin Zhang, Zhu Liu, Zhou Gong, Qiang Wang, Jinbo Huang, Chun Tang, Tingting Zou & Ping Yin

In the Acknowledgements section of this Letter, the second Ministry of Science and Technology grant number should have been 2013CB910200 rather than 2013CB900200; this has been corrected online.